

Robust Two-Qubit Geometric Phase Gates using Amplitude and Frequency Ramping

C. M. Bowers  ^{1,2} D. Palani  ^{1,3} J. J. Barta  ^{1,2} T. H. Guglielmo  ⁴ S. B. Libby  ⁴ D. Leibfried  ¹ and D. H. Slichter  ¹

¹ *National Institute of Standards and Technology, 325 Broadway, Boulder, Colorado 80305, USA*

² *University of Colorado, Boulder, Colorado 80309, USA*

³ *University of Colorado, Denver, Colorado 80204, USA*

⁴ *Lawrence Livermore National Laboratory, Livermore, California 94550, USA*

(Dated: November 19, 2025)

We demonstrate a method for generating entanglement between trapped atomic ions based on adiabatically ramped state-dependent forces. By ramping both the amplitude of the state-dependent force and the motional mode frequencies, we realize an entangling operation that is robust to motional mode occupation and drifts in the mode frequencies. We measure Bell state fidelities above 0.99 across a broad range of ramp parameters and with motional occupations up to 10 phonons. This technique enables high-fidelity entangling operations without ground-state cooling, has a reduced calibration overhead, and is well suited for both quantum logic spectroscopy applications and scalable quantum computing architectures.

The controlled creation of high-fidelity entanglement is crucial for quantum applications across all physical platforms. It is valuable to make this process robust to experimental imperfections or miscalibrations, especially in large-scale quantum systems. Trapped atomic ions possess highly coherent and precisely controllable internal electronic and nuclear degrees of freedom [1–4]. They are typically entangled by coupling these internal (“spin”) states to the ions’ shared motional modes, which can be treated as quantum harmonic oscillators when appropriately cooled. The earliest proposed trapped ion entangling gate required the motional mode be prepared in its ground state, with any motional excitation directly manifesting as entangling gate infidelity [5]. Alternatively, far-off-resonant, state-dependent excitation of the ion motion via static state-dependent forces or instantaneous “kicks” can provide the desired entanglement with reduced sensitivity to the state or coherence properties of the motional mode [6–12].

Currently, geometric phase gates are the most widely used motional-state-insensitive entangling schemes for trapped ions [13–17]. Here, the shared ion motion is coherently displaced along a closed trajectory by a force that depends on the internal states, with each internal state acquiring a geometric phase according to the circumscribed area in phase space. Crucially, the motion must return to its initial state at the end of the entangling operation to eliminate any entanglement between the internal and motional degrees of freedom. While the fidelity of these gates is nominally insensitive to motional mode occupation, various experimental imperfections can prevent perfect closure of motional trajectories, causing gate infidelities that scale with the mode occupation. While this may be tolerable for certain experimental parameters [18–20], in general the highest fidelity demonstrations of geometric phase gates have been done with the motional modes cooled to the ground state, and with careful attention paid to reduce motional decoher-

ence rates and calibrate the motional frequency precisely, including accounting for motional frequency drifts [4, 21–24]. Motional state sensitivity can also be mitigated by modulating the amplitude, phase, and/or frequency of the state-dependent force driving the gate [25–34], by driving state-dependent forces at multiple frequencies [35–41], or through higher-order sidebands [42, 43]. More generally, sensitivities to system parameters can be reduced with the introduction of adiabatic methods, as exemplified by stimulated Raman adiabatic passage (STIRAP) [44]. In large-scale quantum computing architectures, overhead from ground state cooling, cold ion transport, and associated calibrations increases operational complexity and consumes the majority of the time budget in current state-of-the-art quantum algorithms [45, 46]. Reducing the motional-state sensitivity of gate operations may help address these challenges.

In this work, we demonstrate an entangling gate for trapped ions whose fidelity is robust both to motional occupation and to drifts or offsets of the motional frequency. We accomplish this by adiabatically ramping both the amplitude of the state-dependent force (SDF) and the frequency of the motional mode, suppressing errors due to residual spin–motion entanglement. We demonstrate Bell-state fidelities exceeding 0.99 that are independent of motional occupation for up to 10 phonons, well above the Doppler-cooled mode occupation. We also show that the fidelity is reduced by only $\approx 1\%$ when the motional mode frequency is miscalibrated by an amount equal to the inverse of the gate duration. The performance of the gate is insensitive to the exact form of the ramps, as long as they are sufficiently adiabatic. Unlike typical implementations of geometric phase gates, this method does not require joint calibration of the gate duration and detuning between the SDF and motional mode frequency. We perform these entangling gates on two $^{40}\text{Ca}^+$ ions, but we use a driving scheme that is well-suited for use as a mixed-species entangling gate [47–

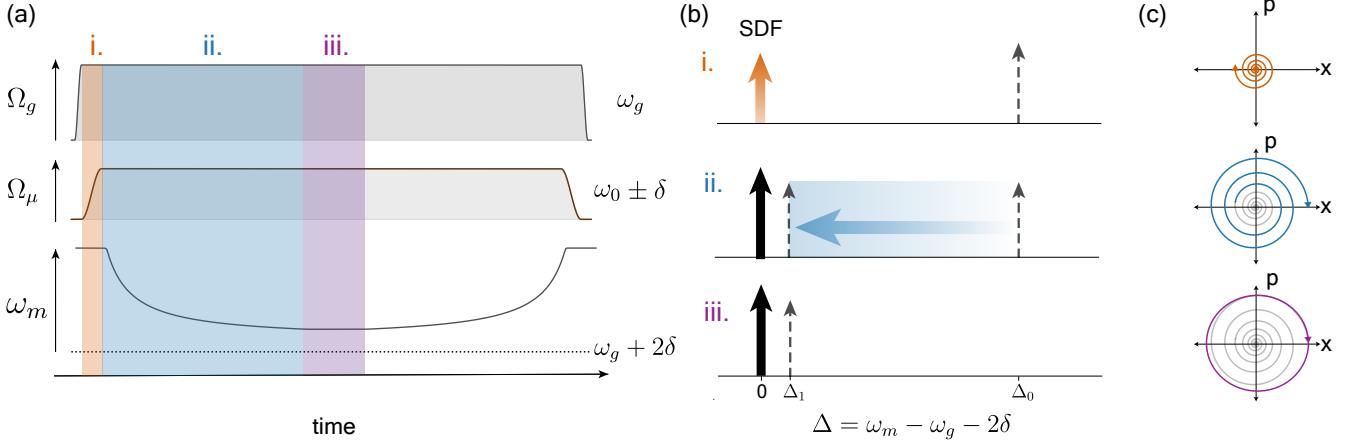


FIG. 1. Gate pulse sequence and motional trajectories. Panel (a) shows the time-dependent amplitude envelopes $\Omega_g(t)$ of the magnetic gradient drive at ω_g (top) and $\Omega_\mu(t)$ of the bichromatic magnetic fields at $\omega_0 \pm \delta$ (middle), as well as the frequency of the motional mode $\omega_m(t)$ (bottom). We plot the detuning Δ between the state-dependent force (thick arrow) and the motional mode (dotted arrow) in (b), and a cartoon of the motional phase space trajectory in (c), for the three highlighted regions in (a). We first ramp on $\Omega_g(t)$ in a time τ_g . Next, in the orange region (i), Ω_μ (and thus the SDF) is ramped on over τ_μ at far-detuned Δ_0 . In the blue region (ii), the motional frequency is ramped from Δ_0 to Δ_1 over duration τ_m . In the purple region (iii), the motional frequency is held constant at Δ_1 , followed by time-reversed versions of all ramps to complete the sequence.

50] in quantum information processing or quantum logic spectroscopy [51]. The drive consists of a strong MHz-frequency oscillating magnetic field gradient combined with weaker microwave-frequency magnetic fields [23, 52]. Adiabatically ramped gates can be used with any gate drive method, but lend themselves naturally to laser-free gate implementations because the increased duration due to ramping does not incur additional spontaneous emission error [53–55].

We consider the gate Hamiltonian for two qubits of frequency ω_0 described by collective spin operators $\hat{S}_i = \hat{\sigma}_{i,1} + \hat{\sigma}_{i,2}$, where the $\hat{\sigma}_{i,k}$ are the Pauli operators ($i \in \{x, y, z\}$) for ion k , and a motional mode with frequency ω_m and ladder operators \hat{a} and \hat{a}^\dagger . We apply a magnetic field gradient oscillating at ω_g (with $\omega_g \sim \omega_m \ll \omega_0$) with strength Ω_g and two homogeneous magnetic fields oscillating at $\omega_0 \pm \delta$ (with $\delta \ll \omega_0$) with strength Ω_μ [23, 52]. Transforming into the interaction picture with respect to $\hbar\omega_0\hat{S}_z + \hbar\omega_m\hat{a}^\dagger\hat{a}$, which we call the “ion frame”, and neglecting fast-rotating terms near $2\omega_0$, gives the gate Hamiltonian [52]

$$H_{\text{ion}} = 2\hbar\Omega_\mu\hat{S}_x \cos(\delta t) + 2\hbar\Omega_g \cos(\omega_g t)\hat{S}_z [\hat{a}e^{-i\omega_m t} + \hat{a}^\dagger e^{i\omega_m t}] \quad (1)$$

The first (“bichromatic”) term drives Rabi oscillations of the qubits with time-dependent Rabi frequency $\Omega_\mu \cos(\delta t)$, while the second (“gradient”) term describes a state-dependent force oscillating at ω_g . Because the two terms do not commute, however, the state-dependent force is modulated by the bichromatic drive. Transforming into the interaction picture with respect to the first term (the “bichromatic” interaction picture) modifies the

state-dependent force, giving [52, 56]

$$\begin{aligned} \hat{H}_I(t) = & 2\hbar\Omega_g \cos(\omega_g t) (\hat{a}e^{-i\omega_m t} + \hat{a}^\dagger e^{i\omega_m t}) \left[\hat{S}_z J_0 \left(\frac{4\Omega_\mu}{\delta} \right) \right. \\ & + 2\hat{S}_z \sum_{n=1}^{\infty} J_{2n} \left(\frac{4\Omega_\mu}{\delta} \right) \cos(2n\delta t) \\ & \left. + 2\hat{S}_y \sum_{n=1}^{\infty} J_{2n-1} \left(\frac{4\Omega_\mu}{\delta} \right) \sin([2n-1]\delta t) \right], \end{aligned} \quad (2)$$

where J_k is the k th Bessel function of the first kind. The modulation of the state-dependent force at ω_g by the non-commuting bichromatic qubit drive spreads the total force over multiple frequencies $\omega_g \pm m\delta$ for integers m , producing either \hat{S}_y (odd m) or \hat{S}_z (even m) interactions. The frame transformation operator between this bichromatic interaction picture and the ion frame is the identity operator as long as the bichromatic term is ramped on and off slowly compared to $1/\delta$ [52]. In this work, we consider the case where Ω_g , Ω_μ , and ω_m are time-dependent and are ramped on and off with durations τ_g , τ_μ , and τ_m , respectively. We choose δ such that the J_2 term is near resonant with ω_m and neglect the other terms, whose impact we consider later. The resulting gate Hamiltonian in the bichromatic interaction picture is then approximately [57]

$$\begin{aligned} \hat{H}_I(t) \approx & 4\hbar \cos(\omega_g t) \cos(2\delta t) \Omega_g(t) J_2 \left(\frac{4\Omega_\mu(t)}{\delta} \right) \\ & \times \hat{S}_z (\hat{a}e^{-i\phi(t)} + \hat{a}^\dagger e^{i\phi(t)}), \end{aligned} \quad (3)$$

where the phase $\phi(t) = \int_0^t \omega_m(t') dt'$ replaces the linear phase accumulation $\omega_m t$ from Eq. (2). This Hamiltonian can be used to produce an effective $\hat{\sigma}_{z,1}\hat{\sigma}_{z,2}$ entangling interaction [23, 57]. The instantaneous detuning of this state-dependent force from the motional frequency is $\Delta(t) = \omega_m(t) - \omega_g - 2\delta$.

In Figure 1(a), we plot $\Omega_g(t)$, $\Omega_\mu(t)$, and $\omega_m(t)$, with the detunings $\Delta(t)$ and schematic motional phase space trajectories for a single qubit state shown in Figs. 1(b) and (c), respectively. The gradient amplitude $\Omega_g(t)$ is ramped on first, with τ_g chosen to minimize spectral content at ω_m to avoid off-resonant motional excitation. Next, the magnetic field amplitude $\Omega_\mu(t)$ is ramped on, with τ_μ chosen to be adiabatic with respect to the detuning from the state-dependent force, $\tau_\mu \Delta \gg 1$, which motivates ramping with the largest practical Δ . Viewed in motional phase space in Fig 1(c), adiabatically ramping Ω_μ in this regime produces spiral trajectories out from the origin at the beginning of the gate pulse and into the origin at end of the gate pulse, which reduces errors due to residual spin-motion entanglement as described theoretically in Refs. [33, 58, 59]. Finally, $\omega_m(t)$ is ramped such that Δ moves from a “far-detuned” regime $\Delta = \Delta_0 \gg \Omega_g J_2(4\Omega_\mu/\delta)$, where the magnetic field is ramped on, to a “near-detuned” one with $\Delta = \Delta_1 \gtrsim \Omega_g J_2(4\Omega_\mu/\delta)$. We require that Δ changes adiabatically, with $\frac{1}{\Delta^2} \frac{d\Delta}{dt} \ll 1$ and $\frac{d\Delta}{dt} = 0$ at the start and end of the ramp. This provides the robustness of a gate operated in the far-detuned or “weak-field” regime [6, 7, 16], with the additional reduction in residual spin-motion entanglement afforded by amplitude ramping [33], but accumulates geometric phase much more rapidly. Any ramp shapes that meet these adiabaticity criteria can be used, affording wide flexibility in implementation. Region (iii) is an optional “flat-top” regime (Ω_g , Ω_μ , and ω_m are constant) whose duration can be adjusted to acquire the desired geometric phase. The ramps are time-reversed after the flat-top region.

We trap two $^{40}\text{Ca}^+$ ions in a surface-electrode ion trap with current-carrying electrodes to produce the strong magnetic field gradient at ω_g and the magnetic fields at $\omega_0 \pm \delta$, as described in [19, 23, 57, 60]. We use the ground state Zeeman sublevels $^2S_{1/2}|m_J = -1/2\rangle \equiv |\downarrow\rangle$ and $^2S_{1/2}|m_J = 1/2\rangle \equiv |\uparrow\rangle$ as a qubit, with a splitting $\omega_0 = 2\pi \times 596$ MHz set by the applied quantization magnetic field of $B_0 \approx 21.3$ mT. The gate is performed on a radial out-of-phase motional mode of the two ions with $\omega_m \approx 2\pi \times 6.8$ MHz, oriented at roughly 20 degrees from the electrode surface normal. Doppler cooling and fluorescence readout are performed using 397 nm laser light resonant with the $^2S_{1/2} \leftrightarrow ^2P_{1/2}$ transition along with 866 nm laser light to repump the $^2D_{3/2}$ level. We use a narrow 729 nm laser to drive the $^2S_{1/2} \leftrightarrow ^2D_{5/2}$ transition for resolved sideband cooling and population shelving prior to readout [61–63]. We cool all four ra-

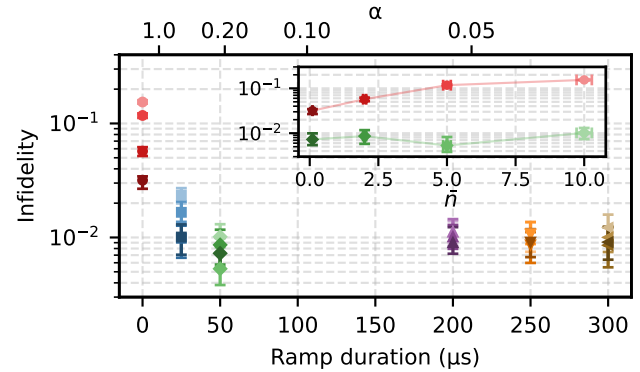


FIG. 2. Bell state infidelity as a function of motional ramp duration and adiabaticity. Points for each ramp duration correspond to initial motional states with mean phonon occupations of $\bar{n} \approx 0, 2, 5$, and 10 , distinguished by progressively lighter shading to indicate increasing \bar{n} . The inset compares the unramped gate (red) with a $50 \mu\text{s}$ ramp (green), illustrating the suppressed dependence of the ramped gate fidelity on the initial phonon occupation.

dial modes close to their ground states using electromagnetically induced transparency (EIT) cooling [64, 65], and both axial modes using resolved sidebands on the $^2S_{1/2} \leftrightarrow ^2D_{5/2}$ transition. We set the fully-ramped-on value of $4\Omega_\mu/\delta \approx 2.405$, near the first zero crossing of J_0 , to increase the qubit coherence through intrinsic dynamical decoupling (IDD) [19, 23, 52]. The motional frequency is ramped by changing the amplitude of the trap rf drive and thus the strength of the pseudopotential confinement [66]. The ramp function is chosen to maintain a constant adiabaticity parameter $\alpha \equiv \frac{1}{\Delta^2} \frac{d\Delta}{dt}$ when ramping from the far detuning Δ_0 to the near detuning Δ_1 . Solving for $\Delta(t)$ gives the general form

$$\Delta(t) = \frac{\Delta_0}{1 - \alpha \Delta_0 t} \quad (4)$$

during the ramp, with the ramp duration fixed by the choice of α to be $\tau_m = \frac{\Delta_0 - \Delta_1}{\alpha \Delta_0 \Delta_1}$. We modify this ramp shape smoothly so the ramp approaches Δ_0 and Δ_1 with $\frac{d\Delta}{dt} = 0$ (see End Matter). The entire gate operation consists of two identical pulse sequences of the type shown in Fig. 1(a) separated by a qubit π_x pulse to implement a spin echo and Walsh modulation [25], preceded and followed by qubit $\pi_x/2$ pulses. This nominally takes the initial state $|\uparrow\uparrow\rangle$ to the Bell state $\frac{1}{\sqrt{2}}(|\downarrow\downarrow\rangle - i|\uparrow\uparrow\rangle)$.

To demonstrate the insensitivity of the ramped gate to motional mode occupation, we characterize Bell state infidelity as a function of τ_m for a range of mean phonon populations, as shown in Fig. 2. The adiabaticity parameter α is plotted on the top axis for each ramp duration according to Eq. (4). We prepare different motional populations using a resonant excitation of the mode whose phase is randomized from shot to shot relative to the

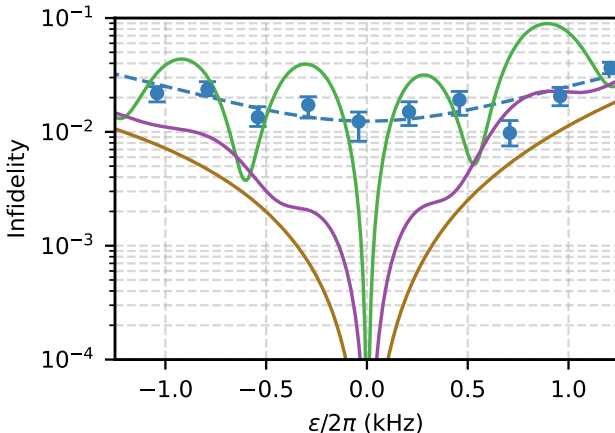


FIG. 3. Bell state infidelity as a function of SDF detuning offset ε for ramped and non-ramped conditions. Experimental data (blue) correspond to a ramped gate with parameters otherwise matching Fig. 2 data with ramp duration $\tau_m = 50 \mu\text{s}$ on a ground-state-cooled ion, with a quadratic fit (dotted blue line). We also plot numerical simulations of an unramped gate (green) and gates with $50 \mu\text{s}$ (purple) and $300 \mu\text{s}$ (brown) motional ramp durations. All numerical simulations were performed in the ion frame and account for all four radial modes. Experimental fidelities are limited by qubit and motional dephasing noise, which is not included in simulations.

SDF (see End Matter). This approach avoids heating the axial modes, which cause increased state readout errors when hot due to our laser beam geometry. The gate begins far detuned with $\Delta_0 = 2\pi \times 153.5 \text{ kHz}$, and the gradient and magnetic fields are ramped sequentially with $\tau_g = 10 \mu\text{s}$ and $\tau_\mu = 30 \mu\text{s}$ with Blackman-Harris envelopes [67]. The motional frequency is then ramped with variable τ_m to $\Delta_1 = 2\pi \times 15 \text{ kHz}$ and back to Δ_0 . For each τ_m , we adjust the flat top duration to optimize Bell state fidelity, with zero ramp duration representing a gate with constant ω_m and $\Delta(t) = \Delta_1$. Bell state fidelity is calculated via population and parity analysis, with uncertainties estimated via nonparametric bootstrapping as in Ref. [23]. We do not correct for state preparation and measurement (SPAM) errors, which are negligible compared to the measured infidelities. The gate becomes progressively less sensitive to the initial average motional occupation \bar{n} as the motional ramps become slower, reaching a roughly constant Bell state infidelity below 10^{-2} for ramp durations $\geq 50 \mu\text{s}$ ($\alpha \leq 0.2$) and \bar{n} up to 10, with a best fidelity of $0.9947^{+0.0015}_{-0.0029}$ at a ramp duration of $50 \mu\text{s}$ and \bar{n} of 5. Faster ramps with $\alpha > 0.2$, as well as gates with no frequency ramping, show increasing infidelity with motional occupation.

Single-loop non-ramped gates with fixed drive strength require a specific relationship between gate detuning and duration to avoid residual spin-motion entanglement, such that mode frequency fluctuations can result in gate

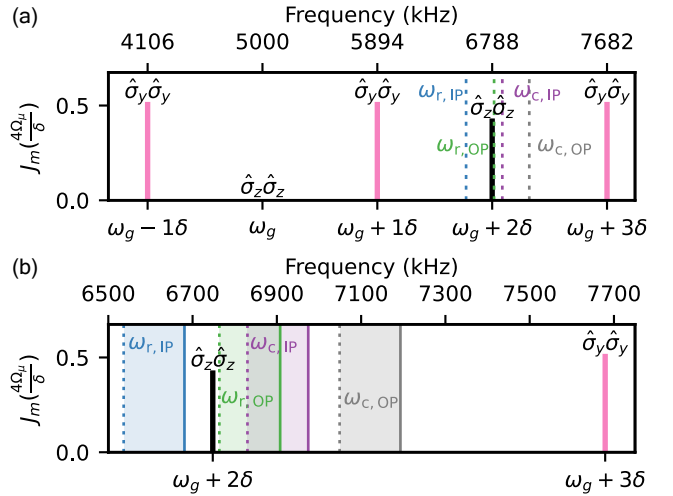


FIG. 4. Spectrum of state-dependent forces in the bichromatic interaction picture. Panel (a) shows the frequencies and relative strengths of the different SDFs at the operating point (pink and black lines), along with the frequencies of the four radial modes at the near-detuned point (dotted lines). Panel (b) shows the range of frequencies spanned by each mode during the ramp, with the solid (dotted) lines indicating the far-detuned (near-detuned) limits of the ramp.

errors [15, 16]. Decoupling duration and detuning in a ramped gate gives robustness to miscalibrations or slow drifts of the mode frequency. It also simplifies calibration by enabling detuning and gate duration to be optimized independently rather than jointly. Figure 3 shows the measured Bell state infidelity for gates with a $50 \mu\text{s}$ motional ramp as a function of an offset ε applied to the bichromatic detuning δ , which mimics the effect of an offset or miscalibration of the motional frequency. The largest values of ε shown are greater than the inverse of the total gate duration (see End Matter). Solid curves show numerical simulations, showing reduced sensitivity to such offsets for ramped gates compared to an unramped gate, with robustness improving for slower ramp rates. The experimental infidelities are higher than the numerically simulated values due to qubit dephasing and motional frequency dephasing. If the other motional modes are not in their ground states during the gate, the cross-Kerr coupling between modes [68, 69] will introduce frequency shifts on the gate mode of a similar form to ε . The magnitude of the shift will depend on the specific confining potential [70]; we measure cross-Kerr shifts on the gate mode of $\lesssim 30 \text{ Hz}$ per phonon in the spectator modes (see End Matter).

Because the two terms of the Hamiltonian in Eq. (1) do not commute, the effective state-dependent force in the bichromatic interaction picture is spread over multiple modulation sidebands at frequencies $\omega_g \pm m\delta$ for integer m , with a modulation index that depends on the strength and detuning of the bichromatic fields (see Eq. 2). The

odd and even sidebands produce effective $\hat{\sigma}_{y,1}\hat{\sigma}_{y,2}$ or $\hat{\sigma}_{z,1}\hat{\sigma}_{z,2}$ interactions, respectively. The SDF spectrum for our experimental parameters of $\omega_g = 2\pi \times 5$ MHz, $\delta = 2\pi \times 894$ kHz, and modulation index $4\Omega_{\mu 0}/\delta \approx 2.405$ is shown in Fig. 4(a), with the near-resonant SDF at $\omega_g + 2\delta$ as in Eq. (3). The frequencies $\omega_{c,IP}$, $\omega_{r,IP}$, $\omega_{c,OP}$, and $\omega_{r,OP}$ of the four motional modes that couple to the SDF—the in-phase “center-of-mass” and out-of-phase “rocking” modes for the in-plane (IP) and out-of-plane (OP) radial direction—are shown as dotted lines. All four modes acquire geometric phases, although the mode at $\omega_{r,OP}$ is dominant; the ramping and detunings of all modes from the SDF help ensure closure of motional trajectories. However, the far-off-resonant $\hat{\sigma}_{y,1}\hat{\sigma}_{y,2}$ interactions do not commute with the $\hat{\sigma}_{z,1}\hat{\sigma}_{z,2}$ interaction, so their coupling to the four motional modes will limit the ultimate fidelity. These are not the limiting errors in our implementation, and it is possible to reduce the resulting infidelity below the 10^{-4} level with suitable δ and motional frequencies. Starting with larger Δ_0 improves robustness and enables faster amplitude ramping, but the off-resonant $\hat{\sigma}_{y,1}\hat{\sigma}_{y,2}$ interactions and the requirement that no modes ramp through resonance with any SDF sidebands set practical limits on the maximum Δ_0 . Fig. 4(b) shows the frequency ranges over which the radial modes are ramped during the gate.

In summary, we demonstrate a high-fidelity, adiabatically ramped $\hat{\sigma}_z\hat{\sigma}_z$ entangling gate that does not require ground-state cooling and is robust to motional-frequency drifts and detuning errors. This relaxes technical requirements and could reduce time and calibration overhead for large-scale quantum systems based on ion shuttling, as well as for quantum logic spectroscopy. The gate scheme we employ is experimentally advantageous for performing mixed-species entangling operations because the SDF can be produced from the same strong gradient plus only a weak bichromatic magnetic field pair for each species. Laser-free mixed-species quantum logic of this form could be used in an architecture where the “data” species does not require any laser light, and the “helper” species requires only low-power resonant lasers for Doppler cooling, state preparation, and readout.

While performing these experiments, we became aware of related work on adiabatically ramped gates [71].

We acknowledge helpful discussions on amplitude and frequency ramped gates with R. T. Sutherland, and initial discussions with D. Hayes, B. Bjork, and S. Erickson. We thank A. L. Carter and P. D. Kent for a careful reading of the manuscript. This work was supported in part by the NIST Quantum Information Program. Part of this work was performed under the auspices of the U.S. Department of Energy by Lawrence Livermore National Laboratory under Contract DE-AC52-07NA27344.

C.M.B., D.P., and D.H.S. conceptualized and planned the experiments. C.M.B. and D.P. carried out the experiments and analyzed the data, with assistance from

J.J.B. and D.H.S.; C.M.B., T.H.G., and D.P. wrote the draft manuscript, and all authors participated in revisions. T.H.G. developed the analytical theory and carried out numerical simulations with assistance from C.M.B.; D.H.S., D.L., T.H.G., and S.B.L. secured funding for the work. D.H.S. supervised the work.

[1] M. C. Marshall, D. A. R. Castillo, W. J. Arthur-Dworschack, A. Aeppli, K. Kim, D. Lee, W. Warfield, J. Hinrichs, N. V. Nardelli, T. M. Fortier, J. Ye, D. R. Leibrandt, and D. B. Hume, *Phys. Rev. Lett.* **135**, 033201 (2025).

[2] M. C. Smith, A. D. Leu, K. Miyanishi, M. F. Gely, and D. M. Lucas, *Phys. Rev. Lett.* **134**, 230601 (2025).

[3] P. Wang, C.-Y. Luan, M. Qiao, M. Um, J. Zhang, Y. Wang, X. Yuan, M. Gu, J. Zhang, and K. Kim, *Nature Communications* **12**, 233 (2021).

[4] C. Löschner, J. Mosca Toba, A. Hughes, S. King, M. Weber, R. Srinivas, R. Matt, R. Nourshargh, D. Allcock, C. Ballance, C. Matthiesen, M. Malinowski, and T. Harty, *PRX Quantum* **6**, 040313 (2025).

[5] J. I. Cirac and P. Zoller, *Phys. Rev. Lett.* **74**, 4091 (1995).

[6] J. I. Cirac and P. Zoller, *Nature* **404**, 579 (2000).

[7] F. Mintert and C. Wunderlich, *Phys. Rev. Lett.* **87**, 257904 (2001).

[8] T. Calarco, J. I. Cirac, and P. Zoller, *Physical Review A* **63**, 062304 (2001).

[9] M. Šašura and A. M. Steane, *Physical Review A* **67**, 062318 (2003).

[10] U. V. Poulsen, S. Sklarz, D. Tannor, and T. Calarco, *Physical Review A* **82**, 012339 (2010).

[11] J. J. García-Ripoll, P. Zoller, and J. I. Cirac, *Phys. Rev. Lett.* **91**, 157901 (2003).

[12] Z. Mehdi, A. K. Ratcliffe, and J. J. Hope, *Physical Review Research* **3**, 013026 (2021).

[13] G. J. Milburn, *Simulating nonlinear spin models in an ion trap* (1999), arXiv:quant-ph/9908037.

[14] E. Solano, R. L. de Matos Filho, and N. Zagury, *Phys. Rev. A* **59**, R2539 (1999).

[15] A. Sørensen and K. Mølmer, *Phys. Rev. Lett.* **82**, 1971 (1999).

[16] A. Sørensen and K. Mølmer, *Phys. Rev. A* **62**, 022311 (2000).

[17] G. Milburn, S. Schneider, and D. James, *Fortschritte der Physik* **48**, 801 (2000).

[18] G. Kirchmair, J. Benhelm, F. Zähringer, R. Gerritsma, C. F. Roos, and R. Blatt, *New Journal of Physics* **11**, 023002 (2009), 0810.0670.

[19] R. Srinivas, *Laser-free trapped-ion quantum logic with a radiofrequency magnetic field gradient*, Ph.D. thesis, University of Colorado Boulder, Boulder, CO (2020).

[20] P. Barthel, P. H. Huber, J. Casanova, I. Arrazola, D. Niroomand, T. Sriarunothai, M. B. Plenio, and C. Wunderlich, *New Journal of Physics* **25**, 063023 (2023).

[21] C. J. Ballance, T. P. Harty, N. M. Linke, M. A. Sepiol, and D. M. Lucas, *Phys. Rev. Lett.* **117**, 060504 (2016).

[22] J. P. Gaebler, T. R. Tan, Y. Lin, Y. Wan, R. Bowler, A. C. Keith, S. Glancy, K. Coakley, E. Knill, D. Leibfried, and D. J. Wineland, *Phys. Rev. Lett.* **117**, 060505 (2016).

[23] R. Srinivas, S. C. Burd, H. M. Knaack, R. T. Sutherland,

A. Kwiatkowski, S. Glancy, E. Knill, D. J. Wineland, D. Leibfried, A. C. Wilson, D. T. C. Allcock, and D. H. Slichter, *Nature* **597**, 209 (2021).

[24] C. R. Clark, H. N. Tinkey, B. C. Sawyer, A. M. Meier, K. A. Burkhardt, C. M. Seck, C. M. Shappert, N. D. Guise, C. E. Volin, S. D. Fallek, H. T. Hayden, W. G. Rellergerd, and K. R. Brown, *Phys. Rev. Lett.* **127**, 130505 (2021).

[25] D. Hayes, S. M. Clark, S. Debnath, D. Hucul, I. V. Inlek, K. W. Lee, Q. Quraishi, and C. Monroe, *Phys. Rev. Lett.* **109**, 020503 (2012).

[26] T. Choi, S. Debnath, T. A. Manning, C. Figgatt, Z. X. Gong, L. M. Duan, and C. Monroe, *Physical Review Letters* **112**, 190502 (2014).

[27] T. J. Green and M. J. Biercuk, *Physical Review Letters* **114**, 120502 (2015).

[28] G. Zarantonello, H. Hahn, J. Morgner, M. Schulte, A. Bautista-Salvador, R. F. Werner, K. Hammerer, and C. Ospelkaus, *Phys. Rev. Lett.* **123**, 260503 (2019).

[29] P. H. Leung, K. A. Landsman, C. Figgatt, N. M. Linke, C. Monroe, and K. R. Brown, *Phys. Rev. Lett.* **120**, 020501 (2018).

[30] C. D. B. Bentley, H. Ball, M. J. Biercuk, A. R. R. Carvalho, M. R. Hush, and H. J. Slatyer, *Advanced Quantum Technologies* **3**, 2000044 (2020).

[31] A. R. Milne, C. L. Edmunds, C. Hempel, F. Roy, S. Mavadia, and M. J. Biercuk, *Phys. Rev. Appl.* **13**, 024022 (2020).

[32] M. Kang, Y. Wang, C. Fang, B. Zhang, O. Khosravani, J. Kim, and K. R. Brown, *Physical Review Applied* **19**, 014014 (2023).

[33] R. Tyler Sutherland and M. Foss-Feig, *New Journal of Physics* **26**, 013013 (2024).

[34] B. P. Ruzic, M. N. Chow, A. D. Burch, D. S. Lobser, M. C. Revelle, J. M. Wilson, C. G. Yale, and S. M. Clark, *Physical Review Applied* **22**, 014007 (2024).

[35] F. Haddadfarshi and F. Mintert, *New Journal of Physics* **18**, 123007 (2016), 1510.05814.

[36] Y. Shapira, R. Shani, T. Manovitz, N. Akerman, and R. Ozeri, *Phys. Rev. Lett.* **121**, 180502 (2018).

[37] A. E. Webb, S. C. Webster, S. Collingbourne, D. Breautaud, A. M. Lawrence, S. Weidt, F. Mintert, and W. K. Hensinger, *Phys. Rev. Lett.* **121**, 180501 (2018).

[38] R. T. Sutherland, R. Srinivas, S. C. Burd, H. M. Knaack, A. C. Wilson, D. J. Wineland, D. Leibfried, D. T. C. Allcock, D. H. Slichter, and S. B. Libby, *Phys. Rev. A* **101**, 042334 (2020).

[39] R. Blümel, N. Grzesiak, N. Pisenti, K. Wright, and Y. Nam, *npj Quantum Information* **7**, 147 (2021).

[40] R. Blümel, N. Grzesiak, N. H. Nguyen, A. M. Green, M. Li, A. Maksymov, N. M. Linke, and Y. Nam, *Physical Review Letters* **126**, 220503 (2021).

[41] M. Orozco-Ruiz, W. Rehman, and F. Mintert, *Phys. Rev. A* **111**, 042404 (2025).

[42] M. Sameti, J. Lishman, and F. Mintert, *Physical Review A* **103**, 052603 (2021).

[43] Y. Shapira, S. Cohen, N. Akerman, A. Stern, and R. Ozeri, *Physical Review Letters* **130**, 030602 (2023).

[44] K. Bergmann, H. Theuer, and B. W. Shore, *Reviews of Modern Physics* **70**, 1003 (1998).

[45] J. M. Pino, J. M. Dreiling, C. Figgatt, J. P. Gaebler, S. A. Moses, M. S. Allman, C. H. Baldwin, M. Foss-Feig, D. Hayes, K. Mayer, C. Ryan-Anderson, and B. Neyenhuis, *Nature* **592**, 209 (2021).

[46] S. A. Moses, C. H. Baldwin, M. S. Allman, R. Ancona, L. Ascarrunz, C. Barnes, J. Bartolotta, B. Bjork, P. Blanchard, M. Bohn, J. G. Bohnet, N. C. Brown, N. Q. Burdick, W. C. Burton, S. L. Campbell, J. P. Campora, C. Carron, J. Chambers, J. W. Chan, Y. H. Chen, A. Chernoguzov, E. Chertkov, J. Colina, J. P. Curtis, R. Daniel, M. DeCross, D. Deen, C. Delaney, J. M. Dreiling, C. T. Ertsgaard, J. Esposito, B. Estey, M. Fabrikant, C. Figgatt, C. Foltz, M. Foss-Feig, D. Francois, J. P. Gaebler, T. M. Gatterman, C. N. Gilbreth, J. Giles, E. Glynn, A. Hall, A. M. Hankin, A. Hansen, D. Hayes, B. Higashi, I. M. Hoffman, B. Horning, J. J. Hout, R. Jacobs, J. Johansen, L. Jones, J. Karcz, T. Klein, P. Lauria, P. Lee, D. Liefer, S. T. Lu, D. Lucchetti, C. Lytle, A. Malm, M. Matheny, B. Mathewson, K. Mayer, D. B. Miller, M. Mills, B. Neyenhuis, L. Nugent, S. Olson, J. Parks, G. N. Price, Z. Price, M. Pugh, A. Ransford, A. P. Reed, C. Roman, M. Rowe, C. Ryan-Anderson, S. Sanders, J. Sedlacek, P. Shevchuk, P. Siegfried, T. Skripka, B. Spaun, R. T. Sprenkle, R. P. Stutz, M. Swallows, R. I. Tobey, A. Tran, T. Tran, E. Vogt, C. Volin, J. Walker, A. M. Zolot, and J. M. Pino, *Phys. Rev. X* **13**, 041052 (2023).

[47] T. R. Tan, J. P. Gaebler, Y. Lin, Y. Wan, R. Bowler, D. Leibfried, and D. Wineland, *Nature* **528**, 380 (2015).

[48] C. J. Ballance, V. M. Schäfer, J. P. Home, D. J. Szwarc, S. C. Webster, D. T. C. Allcock, N. M. Linke, T. P. Harty, D. P. L. A. Craik, D. N. Stacey, A. M. Steane, and D. M. Lucas, *Nature* **528**, 384 (2015).

[49] C. D. Bruzewicz, R. McConnell, J. Stuart, J. M. Sage, and J. Chiaverini, *npj Quantum Information* **5**, 102 (2019), 1905.13122.

[50] A. C. Hughes, V. M. Schäfer, K. Thirumalai, D. P. Nadlinger, S. R. Woodrow, D. M. Lucas, and C. J. Ballance, *Phys. Rev. Lett.* **125**, 080504 (2020).

[51] P. O. Schmidt, T. Rosenband, C. Langer, W. M. Itano, J. C. Bergquist, and D. J. Wineland, *Science* **309**, 749 (2005).

[52] R. T. Sutherland, R. Srinivas, S. C. Burd, D. Leibfried, A. C. Wilson, D. J. Wineland, D. T. C. Allcock, D. H. Slichter, and S. B. Libby, *New Journal of Physics* **21**, 033033 (2019).

[53] R. Ozeri, W. M. Itano, R. B. Blakestad, J. Britton, J. Chiaverini, J. D. Jost, C. Langer, D. Leibfried, R. Reichle, S. Seidelin, J. H. Wesenberg, and D. J. Wineland, *Phys. Rev. A* **75**, 042329 (2007).

[54] I. D. Moore, W. C. Campbell, E. R. Hudson, M. J. Boguslawski, D. J. Wineland, and D. T. C. Allcock, *Physical Review A* **107**, 032413 (2023).

[55] M. J. Boguslawski, Z. J. Wall, S. R. Vizvary, I. D. Moore, M. Bareian, D. T. C. Allcock, D. J. Wineland, E. R. Hudson, and W. C. Campbell, *Physical Review Letters* **131**, 063001 (2023).

[56] C. F. Roos, *New Journal of Physics* **10**, 013002 (2008).

[57] See Supplemental Material for further information.

[58] D. Leibfried, E. Knill, C. Ospelkaus, and D. J. Wineland, *Phys. Rev. A* **76**, 032324 (2007).

[59] H. N. Tinkey, C. R. Clark, B. C. Sawyer, and K. R. Brown, *Phys. Rev. Lett.* **128**, 050502 (2022).

[60] R. Srinivas, S. C. Burd, R. T. Sutherland, A. C. Wilson, D. J. Wineland, D. Leibfried, D. T. C. Allcock, and D. H. Slichter, *Phys. Rev. Lett.* **122**, 163201 (2019).

[61] H. G. Dehmelt, *IEEE Transactions on Instrumentation and Measurement* **IM-31**, 83 (1982).

- [62] F. Diedrich, J. C. Bergquist, W. M. Itano, and D. J. Wineland, *Physical Review Letters* **62**, 403 (1989).
- [63] Ch. Roos, Th. Zeiger, H. Rohde, H. C. Nägerl, J. Eschner, D. Leibfried, F. Schmidt-Kaler, and R. Blatt, *Physical Review Letters* **83**, 4713 (1999).
- [64] G. Morigi, J. Eschner, and C. H. Keitel, *Phys. Rev. Lett.* **85**, 4458 (2000).
- [65] C. F. Roos, D. Leibfried, A. Mundt, F. Schmidt-Kaler, J. Eschner, and R. Blatt, *Physical Review Letters* **85**, 5547 (2000).
- [66] D. J. Wineland, C. Monroe, W. M. Itano, D. Leibfried, B. E. King, and D. M. Meekhof, *J. Res. Natl. Inst. Stand. Technol.* **103**, 259 (1998).
- [67] F. Harris, *Proceedings of the IEEE* **66**, 51 (1978).
- [68] C. F. Roos, T. Monz, K. Kim, M. Riebe, H. Häffner, D. F. V. James, and R. Blatt, *Phys. Rev. A* **77**, 040302 (2008).
- [69] X. R. Nie, C. F. Roos, and D. F. James, *Physics Letters A* **373**, 422 (2009).
- [70] S. Ding, G. Maslennikov, R. Hablützel, and D. Matsukevich, *Phys. Rev. Lett.* **119**, 193602 (2017).
- [71] A. C. Hughes, R. Srinivas, C. M. Löschnauer, H. M. Knaack, R. Matt, C. J. Ballance, M. Malinowski, T. P. Harty, and R. T. Sutherland, *arXiv* , 2510.17286 (2025).
- [72] R. Bowler, U. Warring, J. W. Britton, B. C. Sawyer, and J. Amini, *Review of Scientific Instruments* **84**, 033108 (2013).
- [73] H. M. Knaack, *Laser-Free Operations in a Mixed-Species Trapped Ion Processor*, Ph.D. thesis, University of Colorado Boulder, Boulder, CO (2024).
- [74] K. C. McCormick, J. Keller, D. J. Wineland, A. C. Wilson, and D. Leibfried, *Quantum Science and Technology* **4**, 024010 (2019).
- [75] C. A. Sackett, D. Kielpinski, B. E. King, C. Langer, V. Meyer, C. J. Myatt, M. Rowe, Q. A. Turchette, W. M. Itano, D. J. Wineland, and C. Monroe, *Nature* **404**, 256 (2000).
- [76] DLMF, *NIST Digital Library of Mathematical Functions*, <https://dlmf.nist.gov/>, Release 1.2.4 of 2025-03-15, f. W. J. Olver, A. B. Olde Daalhuis, D. W. Lozier, B. I. Schneider, R. F. Boisvert, C. W. Clark, B. R. Miller, B. V. Saunders, H. S. Cohl, and M. A. McClain, eds.

End Matter

Experiments are performed in a cryogenic surface-electrode trap operated at 10 K, where an rf pseudopotential driven at $\Omega_{\text{RF}}/2\pi \approx 69$ MHz creates the radial confinement. Ions are loaded by photoionization of neutral calcium from a thermal oven, using 423 and 375 nm laser beams. The ions are held 30 μm above the surface of the trap. Doppler cooling and fluorescence readout are performed on the $^2S_{1/2} \leftrightarrow ^2P_{1/2}$ transition using co-propagating 397 nm laser beams with σ^+ and σ^- polarization, along with 866 nm light to repump from the $^2D_{3/2}$ level. Qubit state initialization uses optical pumping into $|\uparrow\rangle$ using the 397 nm σ^+ laser beam. Shelving to the $^2D_{5/2}$ level for state readout is done with a narrow 729 nm laser, which is then depopulated after readout using 854 nm laser light. Readout errors are measured to be at the 10^{-4} level, primarily limited by occasional deshelving from $^2D_{5/2}$ and incomplete repumping from $^2D_{3/2}$. Near-ground-state cooling is achieved using two laser-based methods. The axial center-of-mass and stretch modes at $\omega_{\text{COM}}/2\pi = 2.0$ MHz and $\omega_{\text{STR}}/2\pi = 3.3$ MHz are sideband cooled on the 729 nm transition, while the radial modes are cooled by EIT using a tripod configuration involving the two Zeeman sublevels of $S_{1/2}$ coupled to the $^2P_{1/2} |m_J = 1/2\rangle$ state. The Zeeman splitting of the $^2P_{1/2}$ state is 197 MHz, so the $^2P_{1/2} |m_J = -1/2\rangle$ state is far detuned and can be neglected. The EIT scheme employs a strong σ^+ -polarized beam blue-detuned by 70 MHz from $^2S_{1/2} |m_J = -1/2\rangle \leftrightarrow ^2P_{1/2} |m_J = 1/2\rangle$ and a weak π -polarized probe beam, with the 866 nm repump beam frequency tuned to optimize cooling. EIT cooling exhibits a ≈ 1 MHz cooling bandwidth across the 6.5–7.1 MHz range, enabling simultaneous near-ground-state cooling of all four radial modes with $\bar{n} \approx 0.1$. The magnetic field gradient oscillating at $\omega_g/2\pi = 5$ MHz is generated by three independent phase-synchronized channels of an arbitrary waveform generator (AWG) [19, 60, 72], each driving a current-carrying electrode parallel to the rf electrodes. The relative amplitudes and phases of the currents are tuned to cancel the 5 MHz magnetic field at the ion positions while maximizing the gradient strength, verified by minimizing qubit frequency modulation sidebands at harmonics of ω_g , and by measuring ac Zeeman shifts. The bichromatic magnetic field drive is generated by an amplitude-modulated direct digital synthesizer sources that are amplified and combined on a single current-carrying electrode. Details of the drive electronics are given in Refs. [19, 73].

To enable amplitude modulation of the trap rf drive to ramp the motional frequencies, the output of the signal generator producing the trap rf is split, with one arm going through an amplitude-stabilization circuit and the other going to a mixer. A dc-coupled AWG drives the IF port of the mixer to control the amplitude of the mixer output, which is then amplified and combined with the main amplitude-stabilized rf through the 20 dB forward port of a directional coupler. The resulting combined trap rf is amplified and sent to the trap rf resonator.

Qubit coherence is measured with Ramsey and spin-echo sequences, both with and without IDD [23, 52]. We observe $1/e$ fringe contrast decay times of $T_2^{\text{R}} \approx 600\ \mu\text{s}$ (Ramsey without IDD), $T_2^{\text{E}} \approx 1\ \text{ms}$ (spin echo without IDD), and $T_2^{\text{E,IDD}} \approx 10\ \text{ms}$ (spin echo with IDD). The envelopes of the fringe decay are approximately Gaussian in time, indicating that spin decoherence is dominated by low-frequency qubit frequency fluctuations. We attribute these to environmental magnetic field noise, primarily due to current noise in the coils that generate the quantization magnetic field.

We characterize motional dephasing by measuring the linewidth of the motional modes under weak resonant excitation by an electric field (“tickle”). After cooling near the ground state, we apply a weak, frequency-scanned tickle pulse and probe the addition of a single motional quantum by attempting to drive a motion-subtracting sideband [74]. The narrowest linewidth observed for tickle pulses longer than 2 ms has a full width at half maximum of $\approx 2\pi \times 500$ Hz, which we take as an upper bound on the motional dephasing rate.

For each Bell state fidelity shown, we perform 2,200 individual experimental trials of the entangling operation to analyze the population in the $|\downarrow\downarrow\rangle$, $\{|\uparrow\downarrow\rangle, |\downarrow\uparrow\rangle\}$, and $|\uparrow\uparrow\rangle$ subspaces. Additionally, we perform 5,600 individual experimental trials of the same experiment followed by a qubit $\pi/2$ pulse with 28 different phase values from which we determine the average parity of the resulting state versus phase [75]. The phases are distributed non-uniformly, bunched around values where the parity is near ± 1 .

The parameters Ω_g and Ω_μ used to characterize the strength of the state-dependent force and the bichromatic magnetic field can be expressed as [23, 60]:

$$\begin{aligned}\Omega_g &\equiv \frac{r_0(\hat{r} \cdot \nabla B_g)}{4} \left. \frac{d\omega_0}{dB_z} \right|_{B_z=B_0} \\ \Omega_\mu &\equiv -\frac{B_x}{2\hbar} \langle \downarrow | \mu_x | \uparrow \rangle.\end{aligned}\quad (5)$$

Here ∇B_g is the gradient of the component of the magnetic field oscillating at ω_g along the quantization axis, B_z is the component of the total magnetic field along the quantization axis, B_0 is the applied quantization field, $r_0 = \sqrt{\hbar/(2M\omega_m)}$ is the ground-state extent of the wavefunction for the motional mode along the \hat{r} direction with frequency ω_m for an ion of mass M , B_x is the magnetic field perpendicular to the quantization axis oscillating near ω_0 and μ_x is the component of the ion’s magnetic moment pointed in the same direction.

The detuning $\Delta(t) = \omega_m(t) - \omega_g - 2\delta$ is ramped such that the normalized rate of change remains constant and small:

$$\frac{1}{\Delta^2} \frac{d\Delta}{dt} = \alpha, \quad |\alpha| \ll 1. \quad (6)$$

This defines α , the adiabaticity parameter that describes the speed of the ramp. Solving Eq. (6) for $\Delta(t)$ gives the functional form

$$\frac{d\Delta}{dt} = \alpha \Delta^2 \quad \Rightarrow \quad \Delta(t) = \frac{\Delta_0}{1 - \alpha \Delta_0 t}, \quad (7)$$

In this expression, Δ_0 denotes the initial detuning. The ramp duration required to evolve between two detuning values, Δ_0 and Δ_1 , follows from Eq. (7) and is given by

$$t_m = \frac{1}{\alpha} \left(\frac{1}{\Delta_1} - \frac{1}{\Delta_0} \right). \quad (8)$$

Smaller absolute values of α produce slower ramps that better satisfy the adiabatic condition of Eq. (6). The total waveform is shown in Fig. 1. The experimental hardware is configured such that $\Delta(t)$ is proportional to the voltage output of an AWG, which parameterizes waveforms as a cubic spline [72]. We adjust the spline knots near the start and end of the waveform, increasing the overall ramp duration slightly relative to Eq. (8), to enforce $\frac{d\Delta}{dt} = 0$ at the ramp endpoints while maintaining $\frac{1}{\Delta^2} \frac{d\Delta}{dt} \leq \alpha$ at all times. The ramp durations given in the text include these start and end modifications. The ramp durations of 0, 25, 50, 200, 250, and 300 μs correspond to total durations of the pulse sequence shown in Fig. 1(a) of 468, 505, 527, 698, 718, and 766 μs , respectively. The corresponding total gate durations are then 937, 1011, 1055, 1397, 1437, and 1533 μs .

We prepare different motional occupations for the data in Fig. 2 as follows. All modes of the ion crystal are cooled near their ground states using EIT cooling (radial modes) and resolved sideband cooling (axial modes). Controlled coherent excitation of the gate mode is then applied by resonantly driving a trap electrode. Because the coherent drive is not phase-synchronized to the state-dependent force, each experimental shot realizes a coherent state of motion with displacement $\xi = |\xi| e^{i\theta}$ and randomized phase θ , where we calibrate $|\xi|$ independently. We can then treat the ensemble motional state as a mixed state with density matrix

$$\rho(\xi) = e^{-|\xi|^2} \sum_{n=0}^{\infty} \frac{|\xi|^{2n}}{n!} |n\rangle \langle n| \quad (9)$$

$$= e^{-\bar{n}} \sum_{n=0}^{\infty} \frac{\bar{n}^n}{n!} |n\rangle \langle n| \quad (10)$$

By varying the drive duration, coherent states with different mean phonon occupations $\bar{n} = \text{tr}(\rho \hat{a}^\dagger \hat{a})$ are prepared, corresponding to $\bar{n} = 2.01(6)$, $5.0(1)$, and $10.0(3)$ for the data presented. Alternatively, higher- \bar{n} thermal states could be generated by controlled heating using Doppler beams or broadband noise on a trap electrode from an AWG channel with calibrated bandwidth.

Cross-Kerr coupling arises from anharmonic terms in the trapping potential and introduces mode-mode frequency shifts that depend on mode occupations. They are described by the Hamiltonian $\hat{H}_{\text{Kerr}} = \chi_{a,b} \hat{n}_a \hat{n}_b$, where $\chi_{a,b}$ denotes the coupling strength between modes a and b and the \hat{n} are number operators for the modes [68–70]. We measured these couplings by performing mode frequency spectroscopy with varying coherent excitation of coupled motional modes. For the present trap configuration, the measured couplings are $\chi_{xs,zr} = -28(2)$ Hz/phonon, $\chi_{xs,yr} = -41(3)$ Hz/phonon, and $\chi_{yr,zr} = 9(1)$ Hz/phonon, where xs represents the axial stretch mode and yr and zr correspond to the radial rocking modes aligned predominantly along the y (in-plane) and z (out-of-plane) radial axes. The zr mode is the gate mode (at frequency $\omega_{r,\text{OP}}$).

Supplementary Material for “Robust Two-Qubit Geometric Phase Gates using Amplitude and Frequency Ramping”

DERIVATION OF THE BICHROMATIC HAMILTONIAN

Here we derive the full Hamiltonian of the experimental system described in the main body of the paper, with two ions and four radial modes. We further show how the Hamiltonian can be put into the bichromatic interaction picture with time-dependent $\Omega_\mu(t)$ and $\omega_m(t)$. Our starting point is the lab frame Hamiltonian for two ions interacting with a bichromatic microwave magnetic field and a MHz-frequency magnetic gradient. We include a sum over all four radial oscillator modes, one out-of-phase or STR (s) and one in-phase or COM (c) mode for each radial direction (for this theory supplement we will work with $\hbar = 1$ throughout),

$$\begin{aligned}
H_{\text{lab}}(t) = & \frac{1}{2}\omega_0\hat{S}_{z,c} + \sum_{i=1}^2 \left[\omega_{i,c}(t)\hat{a}_{i,c}^\dagger\hat{a}_{i,c} + \omega_{i,s}(t)\hat{a}_{i,s}^\dagger\hat{a}_{i,s} \right] \\
& + 2\Omega_\mu(t)\hat{S}_{x,c} [\cos((\omega_0 + \delta)t) + \cos((\omega_0 - \delta)t)] \\
& + 2\cos\omega_g t \sum_{i=1}^2 \Omega_{g,i}^{(c)}(t)\hat{S}_{z,c} \left(\hat{a}_{i,c} + \hat{a}_{i,c}^\dagger \right) \\
& + 2\cos\omega_g t \sum_{i=1}^2 \Omega_{g,i}^{(s)}(t)\hat{S}_{z,s} \left(\hat{a}_{i,s} + \hat{a}_{i,s}^\dagger \right), \tag{11}
\end{aligned}$$

where $\hat{a}_{i,c}$ and $\hat{a}_{i,s}$ are the annihilation operators for the two COM modes and the two STR modes, respectively. Each mode has an associated time-dependent motional frequency as well as magnetic gradient Rabi rate Ω_g . The microwave field's Rabi rate Ω_μ is time dependent as well, but is the same for both ions. The spin operators are given by $\hat{S}_{i,c} = \hat{\sigma}_i \otimes \hat{\mathbb{I}} + \hat{\mathbb{I}} \otimes \hat{\sigma}_i$ and $\hat{S}_{i,s} = \hat{\sigma}_i \otimes \hat{\mathbb{I}} - \hat{\mathbb{I}} \otimes \hat{\sigma}_i$ where the $\{\hat{\sigma}_i\}$ are the Pauli matrices. The time dependent Rabi rates and motional frequencies are defined as (for a single arm of the Walsh-1 sequence of length t_f),

$$\begin{aligned}
\Omega_{g,i}^{(c,s)}(t) = \Omega_{g,i}^{(c,s)} & \begin{cases} e_{<g}(t) & 0 \leq t \leq \tau_g \\ 1 & \tau_g < t \leq t_f - \tau_g \\ e_{>g}(t) & t_f - \tau_g < t \leq t_f \end{cases} \\
\Omega_\mu(t) = \Omega_\mu & \begin{cases} 0 & 0 \leq t \leq \tau_g \\ e_{<\mu}(t) & \tau_g < t \leq \tau_g + \tau_\mu \\ 1 & \tau_g + \tau_\mu < t \leq t_f - \tau_g - \tau_\mu \\ e_{>\mu}(t) & t_f - \tau_g - \tau_\mu < t \leq t_f - \tau_g \\ 0 & t_f - \tau_g < t \leq t_f \end{cases} \tag{12} \\
\omega_{i,j}(t) = \omega_{i,j0} + \omega_{i,j1} & \begin{cases} 1 & 0 \leq t \leq \tau_g + \tau_\mu \\ e_{<m}(t) & \tau_g + \tau_\mu < t \leq \tau_g + \tau_\mu + \tau_m \\ 0 & \tau_g + \tau_\mu < t \leq t_f/2 - \tau_g - \tau_\mu - \tau_m \\ e_{>m}(t) & t_f - \tau_g - \tau_\mu - \tau_m < t \leq t_f/2 - \tau_g - \tau_\mu \\ 1 & t_f - \tau_g - \tau_\mu < t \leq t_f \end{cases}
\end{aligned}$$

where $e_{<,>i}$ are the specific envelopes for each ramp. The gradient and microwave fields are ramped according to Blackman-Harris envelopes ($e_{<,>g,\mu}$), while the motional frequency ramp ($e_{<,>m}$) is done in such a way that the ramp speed remains adiabatic at all points with respect to the detuning (details of this ramp are provided in the End Matter of the main body). We will use a sine-squared ramp in this theoretical section as opposed to the true experimental ramps for mathematical simplicity. This is valid as long as the sine-squared ramp is as adiabatic as the experimental ramps.

We now move into the “ion frame” with respect to the internal qubit and motional states. This transformation

operator is given by

$$U_0(t) = \exp\left(-\frac{i}{2}\omega_0 t \hat{S}_{z,c}\right) \prod_{i=1}^2 \exp\left\{-i\hat{a}_{i,c}^\dagger \hat{a}_{i,c} \int_0^t \omega_{i,c}(t') dt'\right\} \exp\left\{-i\hat{a}_{i,s}^\dagger \hat{a}_{i,s} \int_0^t \omega_{i,s}(t') dt'\right\} \quad (13)$$

$$\equiv \exp\left(-\frac{i}{2}\omega_0 t \hat{S}_{z,c}\right) \prod_{i=1}^2 \exp\left(-i\hat{a}_{i,c}^\dagger \hat{a}_{i,c} \phi_{i,c}(t)\right) \exp\left(-i\hat{a}_{i,s}^\dagger \hat{a}_{i,s} \phi_{i,s}(t)\right). \quad (14)$$

The ion frame Hamiltonian is then given by

$$H_{\text{ion}}(t) = U_0^\dagger(t) H_{\text{lab}} U_0(t) + i\dot{U}_0^\dagger(t) U_0(t) \quad (15)$$

$$\begin{aligned} &\approx 2\Omega_\mu(t) \hat{S}_{x,c} \cos \delta t \\ &+ 2 \cos \omega_g t \sum_{i=1}^2 \Omega_{g,i}^{(c)}(t) \hat{S}_{z,c} \left(\hat{a}_{i,c} e^{-i\phi_{i,c}(t)} + \hat{a}_{i,c}^\dagger e^{i\phi_{i,c}(t)} \right) \\ &+ 2 \cos \omega_g t \sum_{i=1}^2 \Omega_{g,i}^{(s)}(t) \hat{S}_{z,s} \left(\hat{a}_{i,s} e^{-i\phi_{i,s}(t)} + \hat{a}_{i,s}^\dagger e^{i\phi_{i,s}(t)} \right) \end{aligned} \quad (16)$$

where fast-oscillating terms near $2\omega_0$ have been dropped. We now go into the “bichromatic frame” with respect to the microwave Hamiltonian H_μ . This transformation operator is

$$U_\mu(t) = \exp\left[-2i\hat{S}_{x,c} \int_0^t \Omega_\mu(t') \cos \delta t' dt'\right] \equiv \exp\left[-i\hat{S}_{x,c} F(t)\right]. \quad (17)$$

Following the analysis in [52], it can be shown that

$$H_{\text{bi}}(t) = U_\mu^\dagger(t) H_{\text{lab}} U_\mu(t) + i\dot{U}_\mu^\dagger(t) U_\mu(t) \quad (18)$$

$$\begin{aligned} &= 2 \cos \omega_g t \sum_{i=1}^2 \Omega_{g,i}^{(c)}(t) \left(\hat{a}_{i,c} e^{-i\phi_{i,c}(t)} + \hat{a}_{i,c}^\dagger e^{i\phi_{i,c}(t)} \right) \left[\hat{S}_{z,c} \cos 2F(t) + \hat{S}_{y,c} \sin 2F(t) \right] \\ &+ 2 \cos \omega_g t \sum_{i=1}^2 \Omega_{g,i}^{(s)}(t) \left(\hat{a}_{i,s} e^{-i\phi_{i,s}(t)} + \hat{a}_{i,s}^\dagger e^{i\phi_{i,s}(t)} \right) \left[\hat{S}_{z,s} \cos 2F(t) + \hat{S}_{y,s} \sin 2F(t) \right] \end{aligned} \quad (19)$$

The general expression for $F(t)$ is fairly complicated. However, the result can be simplified greatly because the bichromatic detuning δ is large compared to the inverse ramp time, $\delta\tau_\mu \gg 1$. If $t \leq \tau_\mu$, the analysis can be continued as

$$F(t \leq \tau_\mu) = 2\Omega_\mu \int_0^t \sin^2 \frac{\pi t'}{2\tau_\mu} \cos \delta t' dt' \quad (20)$$

$$= \frac{\Omega_\mu}{2} \left[\frac{2 \sin \delta t}{\delta} - \frac{1}{\delta} \left(\frac{\sin((\delta - \pi/\tau_\mu)t)}{1 - \frac{\pi}{\delta\tau_\mu}} + \frac{\sin((\delta + \pi/\tau_\mu)t)}{1 + \frac{\pi}{\delta\tau_\mu}} \right) \right] \quad (21)$$

$$\approx \Omega_\mu \frac{\sin \delta t}{\delta} \left[1 - \cos \frac{\pi t}{\tau_\mu} \right] \quad (22)$$

$$= \Omega_\mu \frac{2 \sin \delta t}{\delta} \sin^2 \frac{\pi t}{2\tau_\mu} = \frac{2\Omega_\mu(t) \sin \delta t}{\delta}, \quad (23)$$

where we expanded the denominators in (21) using the geometric series and truncated the series at first order. This approximation is valid for our experimental parameters. Extending the integration to all times from $t \leq \tau_\mu$ in Eq. (20) is straightforward, and the result is unchanged,

$$F(t) = \frac{2\Omega_\mu(t) \sin \delta t}{\delta}. \quad (24)$$

With this simplified form, we can now perform the Jacobi-Anger expansion on Eq. (19) to yield

$$H_{\text{bi}}(t) \approx 2 \cos \omega_g t \sum_{i=1}^2 \Omega_{g,i}^{(c)}(t) \left(\hat{a}_{i,c} e^{-i\phi_{i,c}(t)} + \hat{a}_{i,c}^\dagger e^{i\phi_{i,c}(t)} \right) \left\{ \hat{S}_{z,c} \left[J_0 \left(\frac{4\Omega_\mu(t)}{\delta} \right) + 2 \sum_{n=1}^{\infty} J_{2n} \left(\frac{4\Omega_\mu(t)}{\delta} \right) \cos 2n\delta t \right] \right. \\ \left. + 2\hat{S}_{y,c} \sum_{n=1}^{\infty} J_{2n-1} \left(\frac{4\Omega_\mu(t)}{\delta} \right) \sin[(2n-1)\delta t] \right\} \\ + 2 \cos \omega_g t \sum_{i=1}^2 \Omega_{g,i}^{(s)}(t) \left(\hat{a}_{i,s} e^{-i\phi_{i,s}(t)} + \hat{a}_{i,s}^\dagger e^{i\phi_{i,s}(t)} \right) \left\{ \hat{S}_{z,s} \left[J_0 \left(\frac{4\Omega_\mu(t)}{\delta} \right) + 2 \sum_{n=1}^{\infty} J_{2n} \left(\frac{4\Omega_\mu(t)}{\delta} \right) \cos 2n\delta t \right] \right. \\ \left. + 2\hat{S}_{y,s} \sum_{n=1}^{\infty} J_{2n-1} \left(\frac{4\Omega_\mu(t)}{\delta} \right) \sin[(2n-1)\delta t] \right\} \quad (25)$$

$$\approx 4 \cos \omega_g t \cos 2\delta t J_2 \left(\frac{4\Omega_\mu(t)}{\delta} \right) \sum_{i=1}^2 \left[\Omega_{g,i}^{(c)}(t) \hat{S}_{z,c} \left(\hat{a}_{i,c} e^{-i\phi_{i,c}(t)} + \hat{a}_{i,c}^\dagger e^{i\phi_{i,c}(t)} \right) \right. \\ \left. + \Omega_{g,i}^{(s)}(t) \hat{S}_{z,s} \left(\hat{a}_{i,s} e^{-i\phi_{i,s}(t)} + \hat{a}_{i,s}^\dagger e^{i\phi_{i,s}(t)} \right) \right], \quad (26)$$

where in Eq. (26) we selected the resonant J_2 term. For a single motional mode, this reduces to

$$H_{\text{bi, single}} \approx 4 \cos \omega_g t \cos 2\delta t \Omega_g(t) J_2 \left(\frac{4\Omega_\mu(t)}{\delta} \right) \hat{S}_z \left(\hat{a} e^{-i\phi(t)} + \hat{a}^\dagger e^{i\phi(t)} \right). \quad (27)$$

ANALYTICAL MODEL OF A MOTIONALLY RAMPED GATE WITHOUT AMPLITUDE RAMPING

Next we derive an analytical model to gain some intuition for the physics of the ramped gate, and in particular how the residual spin-motion entanglement is adiabatically eliminated through motional frequency ramping. Solving for the exact dynamics of Eq. (19) analytically is not possible, but we can learn about some approximate scalings under certain assumptions starting from Eq. (27). We begin by assuming that Ω_g and Ω_μ are constant, and that the motional frequency is ramped according to a \cos^2 function over the entire duration of the gate without a flat-top. The amplitude ramping, which is lost in this approximation and is described in Ref. [33], is a crucial part of the robustness of the gate, as verified by numerical simulations. However, the impact of the frequency ramping alone can nonetheless be seen in the following analytical derivation even without amplitude ramping. We emphasize that this is not a complete analytical solution for the dynamics of the experimentally demonstrated gates. The replacement of the adiabatic frequency ramp discussed in the main text by a \cos^2 frequency ramp is justified as long as we maintain the adiabatic condition, $\frac{1}{\Delta\omega} \frac{d\Delta}{dt} \leq \alpha_{\text{max}}$, where $\alpha_{\text{max}} \ll 1$. This adiabatic condition is easily achieved with parameters relevant to the experimental configuration described in the main text.

We assume $\omega_m(t) = \omega_{m0} + \omega_{m1} \cos^2(\pi t/t_f)$, and $\phi(t) = \omega_{m0}t + \omega_{m1} \int_0^t \cos^2(\pi t'/t_f) dt'$. We take the gate to occur over the time interval $t \in [0, t_f]$ and define $\phi(t) \equiv \omega_{m0}t + \omega_{m1}\Xi(t)$. Substituting into Eq. (27) gives

$$H_{bi}(t) = 4 \cos \omega_g t \cos 2\delta t \Omega_g J_2 \left(\frac{4\Omega_\mu}{\delta} \right) \hat{S}_z \left[\hat{a} e^{-i\omega_{m0}t} e^{-i\omega_{m1}\Xi(t)} + \hat{a}^\dagger e^{i\omega_{m0}t} e^{i\omega_{m1}\Xi(t)} \right]. \quad (28)$$

We require that $2\delta \approx \omega_{m0} - \omega_g$ and $\omega_{m1} \ll \delta$ to comply with the assumptions underlying Eq. (27). The Hamiltonian is then approximately given by

$$H_{bi}(t) \approx \Omega_\phi \hat{S}_z \left[\hat{a}^\dagger e^{i(\omega_{m0} - \omega_g - 2\delta)t} e^{i\omega_{m1}\Xi(t)} - \hat{a} e^{-i(\omega_{m0} - \omega_g - 2\delta)t} e^{-i\omega_{m1}\Xi(t)} \right] \quad (29)$$

$$= \Omega_\phi \hat{S}_z \left[\hat{a}^\dagger e^{i(\omega_{m0} - \omega_g - 2\delta + \omega_{m1}/2)t} e^{\frac{i\omega_{m1}t_f}{4\pi} \sin \frac{2\pi t}{t_f}} - \hat{a} e^{-i(\omega_{m0} - \omega_g - 2\delta + \omega_{m1}/2)t} e^{-\frac{i\omega_{m1}t_f}{4\pi} \sin \frac{2\pi t}{t_f}} \right]$$

$$\equiv \Omega_\phi \hat{S}_z \left[\hat{a}^\dagger e^{i\bar{\Delta}t} e^{\frac{i\omega_{m1}t_f}{4\pi} \sin \frac{2\pi t}{t_f}} - \hat{a} e^{-i\bar{\Delta}t} e^{-\frac{i\omega_{m1}t_f}{4\pi} \sin \frac{2\pi t}{t_f}} \right] \quad (30)$$

where $\bar{\Delta} \equiv \omega_{m0} - \omega_g - 2\delta + \omega_{m1}/2$, and $\Omega_\phi = \Omega_g J_2(4\Omega_\mu/\delta)$.

Computing the displacement, $\xi(t)$

Writing the Magnus expansion to second order (which is exact for this Hamiltonian) allows us to write the propagator for (30) as

$$U_{\text{bi}}(t) = \exp \left[-i (\xi(t) \hat{a}^\dagger + \xi^*(t) \hat{a}) \hat{S}_z \right] \exp \left(-i \theta(t) \hat{S}_z^2 \right), \quad (31)$$

where $\xi(t)$ is a complex-valued function describing the amplitude of the state-dependent displacement and $\theta(t)$ is a real-valued function expressing the geometric phase acquired. The first exponential, the state dependent force (SDF), provides a coupling between motional modes and the spin degrees of freedom, while the second exponential generates entanglement between the spin degrees of freedom in a $\hat{\sigma}_z \otimes \hat{\sigma}_z$ gate interaction. The ideal implementation of the gate has $\xi(t_f) = 0$ (no residual spin-motion entanglement at the end of the gate) and $\theta(t_f) = \pi/8$ (correct geometric phase to take an unentangled initial spin state to a Bell state). Focusing on the SDF, we find that the displacement obeys the integrable ODE,

$$\dot{\xi}(t) = \Omega_\phi e^{i\bar{\Delta}t} \exp \left[\frac{i\omega_{m1}t_f}{4\pi} \sin \frac{2\pi t}{t_f} \right]. \quad (32)$$

To proceed with the integration, we consider the end of the gate when $t = t_f$, and define a few quantities to make the notation easier,

$$\xi(t) = \frac{\Omega_\phi t_f}{2\pi} \int_0^{2\pi t_f} \exp \left[i \left(\frac{\bar{\Delta}t_f}{2\pi} u + \frac{\omega_{m1}t_f}{4\pi} \sin u \right) \right] du \quad (33)$$

$$\xi(t_f) = \frac{\Omega_\phi t_f}{2\pi} \int_0^{2\pi} \exp[i(\mu u + x \sin u)] du \quad (34)$$

$$= \frac{\Omega_\phi t_f}{2\pi} \left\{ \int_0^\pi \exp[i(\mu u + x \sin u)] du + \int_0^\pi \exp[i(\mu(2\pi - u) + x \sin(2\pi - u))] du \right\} \quad (35)$$

$$= \frac{\Omega_\phi t_f}{2\pi} \left\{ \int_0^\pi \exp[i(\mu u + x \sin u)] du + e^{2\pi i \mu} \int_0^\pi \exp[-i(\mu u + x \sin u)] du \right\} \quad (36)$$

$$= \frac{\Omega_\phi t_f}{2\pi} \left\{ \int_0^\pi \cos(-\mu u - x \sin u) du - i \int_0^\pi \sin(-\mu u - x \sin u) du + e^{2\pi i \mu} \int_0^\pi \cos(-\mu u - x \sin u) du + i e^{2\pi i \mu} \int_0^\pi \sin(-\mu u - x \sin u) du \right\} \quad (37)$$

where $x = \omega_{m1}t_f/(4\pi)$ and $\mu = \bar{\Delta}t_f/(2\pi)$.

We can now make use of the definition of Anger-Weber functions [76] to write

$$\xi(t_f) = \frac{\Omega_\phi t_f}{2} [(1 + e^{2\pi i \mu}) \mathbf{J}_{-\mu}(x) - i(1 - e^{2\pi i \mu}) \mathbf{E}_{-\mu}(x)] \quad (38)$$

$$= \Omega_\phi t_f e^{i\pi\mu} [\cos \pi\mu \mathbf{J}_{-\mu}(x) - \sin \pi\mu \mathbf{E}_{-\mu}(x)] \quad (39)$$

$$= \Omega_\phi t_f e^{i\pi\mu} \mathbf{J}_\mu(x), \quad (40)$$

where $\mathbf{J}_\beta(z)$ and $\mathbf{E}_\beta(z)$ are Anger and Weber functions of order β , respectively. Now, we can attempt to understand the asymptotics of this function. First, we substitute in the actual parameters that compose μ and x . Defining a few

more quantities,

$$2\pi d_f \equiv \Delta_0 = \omega_{m0} + \omega_{m1} - \omega_g - 2\delta \quad (41)$$

$$2\pi d_n \equiv \Delta_1 = \omega_{m0} - \omega_g - 2\delta \quad (42)$$

$$\implies \bar{\Delta} = 2\pi \frac{d_f + d_n}{2} \quad (43)$$

$$\implies \mu = \frac{d_f + d_n}{2} t_f \quad (44)$$

$$\implies x = \frac{d_f - d_n}{2} t_f \quad (45)$$

where we have introduced the quantities d_f , the initial far detuning, and d_n , the final near detuning, which have units of frequency (not angular frequency). Now, plugging these expressions into (40) we find,

$$\xi(t_f) = \Omega_\phi t_f e^{i\pi\mu} \mathbf{J}_{(d_f + d_n)t_f/2} \left(\frac{(d_f - d_n)t_f}{2} \right) \quad (46)$$

$$= \Omega_\phi t_f e^{i\pi\mu} \mathbf{J}_{(d_f + d_n)t_f/2} \left(\lambda \frac{(d_f + d_n)t_f}{2} \right) \quad (47)$$

$$\equiv \Omega_\phi t_f e^{i\pi\mu} \mathbf{J}_\mu(\lambda\mu) \quad (48)$$

where $\lambda \equiv (d_f - d_n)/(d_f + d_n)$ and $\mu \equiv (d_f + d_n)t_f/2$. We now fix λ , and see how \mathbf{J} scales with μ – this is equivalent to understanding the scaling with respect to gate duration t_f for fixed near and far detunings d_n and d_f . We will now be working in limit $\mu \gg 1$, which corresponds to multiple loops in phase space over the course of the gate. To understand this asymptotic expansion, we can rewrite the Anger function as

$$\mathbf{J}_\mu(\lambda\mu) = J_\mu(\lambda\mu) + \sin \pi\mu \mathbf{A}_\mu(\lambda\mu) \quad (49)$$

where J_μ is a standard Bessel function of the first kind and \mathbf{A}_μ is an associated Anger-Weber function. We can now use the asymptotic expansion for \mathbf{A}_μ when μ is large and λ is fixed. Our expansion can then be written as [76]

$$\mathbf{J}_\mu(\lambda\mu) \sim J_\mu(\lambda\mu) + \frac{\sin \pi\mu}{\pi} \sum_{k=0}^{\infty} \frac{(2k)! a_k(\lambda)}{\mu^{2k+1}} . \quad (50)$$

$$a_0 = \frac{1}{1 + \lambda} \quad (51)$$

$$a_1 = \frac{-\lambda}{2(1 + \lambda)^4} \dots \quad (52)$$

Truncating the sum to first order is a very good approximation in our operating regime:

$$\mathbf{J}_\mu(\lambda\mu) \sim J_\mu(\lambda\mu) + \frac{\sin \pi\mu}{\pi\mu} \frac{1}{1 + \lambda} \quad (53)$$

$$= J_\mu(\lambda\mu) + \frac{\sin \pi\mu}{\pi d_f t_f} \quad (54)$$

Now, substituting (54) into (48) our asymptotic expansion for ξ is now

$$\xi(t_f) \sim \Omega_\phi t_f e^{i\pi\mu} \left[J_\mu(\lambda\mu) + \frac{\sin \pi\mu}{\pi d_f t_f} \right] . \quad (55)$$

We can simplify this using the Debye expansion for J_μ . Focusing on $J_\mu(\lambda\mu)$ and defining $\lambda \equiv \operatorname{sech} \beta$, we have

$$J_\mu(\lambda\mu) \sim \frac{e^{\mu(\tanh \beta - \beta)}}{\sqrt{2\pi\mu \tanh \beta}} \left(1 + \frac{1}{24} \frac{3 \coth \beta - 5 \coth^3 \beta}{\mu} + \dots \right) . \quad (56)$$

Again truncating the sum to the first term,

$$\tanh \beta = \frac{2\sqrt{d_f d_n}}{d_f + d_n} \quad (57)$$

$$\tanh \frac{\beta}{2} = \sqrt{\frac{d_n}{d_f}} \quad (58)$$

$$\implies \beta = 2 \operatorname{atanh} \sqrt{\frac{d_n}{d_f}}, \quad (59)$$

and putting it all together, we find

$$\implies J_\mu(\lambda\mu) \sim \frac{\exp \left[2\mu \left(\frac{\sqrt{d_f d_n}}{d_f + d_n} - \operatorname{atanh} \sqrt{\frac{d_n}{d_f}} \right) \right]}{\sqrt{2\pi\mu \frac{2\sqrt{d_f d_n}}{d_f + d_n}}} \quad (60)$$

$$= \frac{\exp \left[t_f \left(\sqrt{d_f d_n} - (d_f + d_n) \operatorname{atanh} \sqrt{\frac{d_n}{d_f}} \right) \right]}{\sqrt{2\pi t_f \sqrt{d_f d_n}}}. \quad (61)$$

Substituting (61) into (55) we arrive at the final form of the truncated expansion for $\xi(t_f)$,

$$\xi(t_f) \sim \Omega_\phi e^{i\pi\mu} \left\{ \sqrt{\frac{t_f}{2\pi\sqrt{d_f d_n}}} \exp \left[t_f \left(\sqrt{d_f d_n} - (d_f + d_n) \operatorname{atanh} \sqrt{\frac{d_n}{d_f}} \right) \right] + \frac{\sin \pi\mu}{\pi d_f} \right\}. \quad (62)$$

With $d_n < d_f$, the first term in the curly brackets is exponentially suppressed and can be neglected as long as $t_f d_n \sqrt{d_n/d_f} \gg 1$, which corresponds to the gate performing multiple loops in motional phase space. The second term is an oscillating sine, which for fixed d_f has a constant amplitude. However, it shows that the worst-case final displacement scales inversely with the initial far detuning ($\xi(t_f) \propto 1/d_f$), as opposed to $\xi(t_f) \propto 1/d_n$ for a typical near detuned gate. Thus, increasing the far detuning d_f reduces the residual spin-motional entanglement at the end of the gate.

To quantify how this residual spin-dependent displacement contributes to gate infidelity, we assume that the state starts in a motional Fock state $|n\rangle$ and then compute the final infidelity with respect to this same Fock state, and average over all initial pure spin states in SU(4). In the regime where $|\xi(t_f)| \ll 1$, then the infidelity is

$$\mathcal{I} \approx |\xi(t_f)|^2 (2n + 1) \lambda_{S_z}^2 \quad (63)$$

$$= \frac{8}{5} |\xi(t_f)|^2 (2n + 1), \quad (64)$$

where $\lambda_{S_z}^2$ is the variance of S_z and is equal to $8/5$ when averaged over SU(4) (an average over all initial pure states). Hence, the infidelity scales as $1/d_f^2$, which can be a substantial enhancement when working at large far detunings. Additionally, working with larger d_n and t_f exponentially reduces the contribution of the first term in (62). Although this model does not include amplitude ramping, which is crucial for the full robustness of the gate, it does offer insight into the impact of frequency ramping and desirable parameter regimes for operation.